

# **The Stellar Content and Star Formation History of the late-type spiral galaxy NGC 300 from *Hubble Space Telescope*<sup>1</sup>observations**

D. J. Butler, D. Martínez-Delgado

and

W. Brandner

Max-Planck-Institut für Astronomie, Königstuhl 17, D-69117 Heidelberg, Germany

`butler@mpia.de, ddelgado@mpia.de, brandner@mpia.de`

Received \_\_\_\_\_; accepted \_\_\_\_\_

Accepted by AJ

## ABSTRACT

We present the first WFPC2 V, I photometry for the Sculptor Group galaxy NGC 300 in four fields ranging from the centre to the outer edge. We have made the first measurement of the star formation histories in two disk fields: the oldest stars were born at similar epochs and formation activity increased but at different mean rates. The main disk stellar population is predominantly old, consisting of RGB and AGB stars, based on a synthetic colour magnitude diagram analysis.  $Z$  is found to have been more metal poor than  $0.006$  (or  $0.33 Z_{\odot}$ ) with no evidence for significant change in the mean  $Z$  value over time in both disk fields. In the central region, we find a dearth of bright stars with respect to the two disk fields that cannot be explained by observational effects. Taken at face value, this finding would agree with the Davidge (1998) report of suppressed star formation there during the past  $10^9$  yr with respect to his disk fields at larger radii; but the possibility of significant central extinction affecting our finding remains. We have also determined the first distance modulus estimate based on the tip of the red giant branch method: on the Cepheid distance scale of Ferrarese et al. (2000) we find  $(m-M)_0 = 26.56 \pm 0.07$  ( $\pm 0.13$ ) mag; and a similar value from the Cepheid-independent empirical method by Lee et al. (1993), both in good agreement with the Cepheid distance determined by Freedman et al. (2001). A discrepancy with the theoretical calibration of the red giant branch tip magnitude method remains. Finally, we report a newly detected young (up to about 10 Myr) stellar association of about average size ( $\sim 140$  pc) in one of the disk fields.

*Subject headings:* galaxies: spiral – galaxies: distance – galaxies: formation – galaxies: star formation – optical: galaxies

## 1. Introduction

In recent years real observational evidence has emerged indicating that spiral galaxies assembled their components (disk, halo, bulge) at different times and on different timescales (for example, Andredakis, Peletier & Balcells 1995; Ibata et al. 2001, and references therein; and Gratton et al. 2003, based on ages of a small sample of three Milky Way globular clusters). Galaxy formation studies are usually performed using surveys; however, it is of obvious importance to take representative examples of Hubble types and to study them in detail. In order to learn about galaxy formation and evolution in detail, there are three basic diagnostic tools, namely morphology, kinematics and stellar populations. Of these, perhaps the most direct way of studying the evolution of a galaxy's stellar component is with diffraction limited imaging, using the Hubble Space Telescope (HST).

NGC 300 is typical of a late-type spiral of type SA(s)d (Tully 1988) and the brightest of five main spiral galaxies that compose the Sculptor group. With a Cepheid-based distance estimate of  $(m-M)_0 = 26.53 \pm 0.07$  mag (Freedman et al. 2001) and its near face-on orientation, NGC 300 is well suited to studies of its stellar content. In the past decade, many studies have been devoted to study the bright young stellar population in this galaxy. Consequently, there are now several signs pointing to recent massive star formation, namely the presence Wolf-Rayet stars (e.g. Schild et al. 2003) and individual supergiants (Urbaneja et al. 2003; Bresolin et al. 2002a/b; Schild & Testor 1992; Humphreys et al. 1986; Massey et al. 1984), young stellar associations (Pietryński et al. 2001), Cepheids (Pietryński et al. 2002), H<sub>II</sub> regions (e.g. Soffner et al. 1996, DeHarveng et al. 1988),

---

<sup>1</sup>Based on observations made with the NASA/ESA Hubble Space Telescope, obtained from the data archive at the Space Telescope Science Institute. STScI is operated by the Association of Universities for Research in Astronomy, Inc. under NASA contract NAS 5-26555.

supernova remnants (Pannuti et al. 2000), and X-ray emission (Read & Pietsch 2001). The older stellar populations have also been targeted (see Davidge 1998 and references therein) but high angular resolution imaging ( $\lesssim 0.05''$ ) is needed to probe this fainter stellar population.

In this paper, we present the first study of the resolved old, intermediate-age and young stellar population of the spiral galaxy NGC 300 based on colour-magnitude diagrams (CMDs) from HST observations. The main motivation for optical imaging data is sensitivity to a relatively wide range of temperatures in non- or marginally extincted fields. This paper is composed as followed. Data and data reduction are described in Sec. 2. An overview of the stellar populations based on CMDs is given in Sec. 3. The distance measurement based on the tip magnitude of the red giant branch is described in Sec. 4, and the issue of internal extinction is discussed in Sec. 5. The derivation of the chemical enrichment and star formation history is presented in Sec. 7. Finally, we discuss our findings in Sec. 8, and summarize them in Sec. 9.

## 2. Data and data reduction

For this study, we retrieved the calibrated science and data quality images of several NGC 300 fields from the Space Telescope Science Institute HST data archive. We have examined archive I<sub>814</sub>- and V<sub>547/555/606</sub>-band frames from four HST/WFPC2 pointings. These are listed in Table 1, and their WFPC2 footprints are superimposed on an image from the ESO Wide Fielder Imager (hereafter referred to as ESO/WFI<sup>2</sup>) in Fig. 1. Data reduction details are given by Baggett et al. (2002) and Holtzman et al. (1995).

The photometry of the stars in NGC 300 was derived using the HSTPHOT (Dolphin

---

<sup>2</sup>See Pietrzynski et al. (2002) for observation details.

2000a) point spread function (PSF)-fitting photometry package which is designed for optimal reduction and analysis of WFPC2 data, and has been used recently in a number of stellar population studies (e.g. Méndez et al. 2002, and references therein). The code utilizes a library of PSFs to account for PSF position dependence, and is optimized for the undersampled PSFs present in WFPC2 data. This package was also used to mask bad pixels and columns using the data-quality image and reject cosmic rays in the images. For transformation of the WFPC2 photometry into the standard V-, I-band system, stellar magnitudes are calibrated by HSTphot using the charge transfer efficiency and zero point magnitude corrections derived by Dolphin (2000b). The package is reported to be accurate to 0.02 mag Dolphin (2000) with a coordinate transformation rms residuals of the order of 0.02" in both axes.

Artificial star tests have been performed using HSTphot for the V-band magnitude range 20 to 28 (mag) and  $V-I = -0.5$  to 3 (mag) which are approximately the ranges interest in our CMDs. Each test consisted of choosing a star from the V-band magnitude and colour range, adding it to both the V, and I-band images and then the image was reanalyzed by HSTphot. In this way, the effect of creating additional crowding of stars has been minimized. This was repeated several thousand times for each WFPC2 frame. From all of the tests a database of measurements for different positions and input V-band magnitudes and colours is built. The ratio of the number of recovered stars to the number of added stars in a magnitude range indicates the statistical probability of recovering a star in that magnitude range. Additionally, the database allows the photometry errors (recovered - input magnitudes) to be determined for each bandpass.

Fig. 2 plots the completeness factor against magnitude for our four fields situated at different radial distances from the centre of NGC 300. A completeness plateau occurs for the brightest stars because their signal-to-noise is sufficiently high and crowding affects

these stars equally. A completeness of 100% is not reached because of bad pixels.<sup>3</sup> For each band pass, the completeness is different at each pointing. The F4 field has the longest integration time, providing the faintest magnitude limit and the crowding factor is shifted accordingly to fainter magnitudes relative to the other integrations. There is a strong difference between the functions of the innermost and outermost fields. Indeed, detectability in the inner field is less efficient than in the outer fields largely due to severe crowding, as well as shorter integration times. The V-band functions have fainter limiting magnitudes than in I-band largely because of lower HST/WFPC-2 throughput in the I<sub>814</sub>-band.

For the final photometry list used in this study, we select those objects flagged as valid stars in both band-passes and have  $S/N > 5$ ;  $\chi^2 < 5$ ;  $-0.5 < \text{sharpness} < 0.5$ ; and  $\sigma_{V,I} < 0.25 \text{ mag}$ . After selection, there are 7614, 1421, 3467 and 235 stars in the F1, F2, F3 and F4 fields respectively. In the present paper we apply the selection criteria to stars at  $I < 23 \text{ mag}$  whenever star counts in colour magnitude diagrams are analyzed. At this magnitude limit and brighter, the artificial star tests find the data to be at least 90% complete, and stars intrinsically brighter than  $I = 23 \text{ mag}$  will only be missed if they are physically obscured, e.g. by dust.

### 3. The stellar content of NGC 300 from the colour-magnitude diagram

Fig 3 shows the CMDs for the four WFPC2 fields described in Table 1. These fields occur at radial distances ranging from  $0.44'$  to  $12.8'$  or de-projected radial distances of 0.4 to 10.9 kpc at the distance of the NGC 300 for a distance of  $2.02 \text{ Mpc} \pm 0.07$  (Freedman et

---

<sup>3</sup>The number of pixels deemed to be bad in the unvignetted portion of each chip/frame is of the order of 1% (includes cosmic ray events; and includes columns and pixels flagged as bad in the STScI data quality file).

al. 2001).

The F1 and F3 fields overlap with parts of different spiral arms in NGC 300 (see Fig 1) and the CMD of each region provide a sketch of some of the stellar content there. The most prominent feature is the red giant branch (RGB) structure, which is very similar to those observed in nearby dwarf irregular galaxies (NGC 6822: Gallart et al. 1996; Sextans A: Dohm-Palmer et al. 2002). This structure is typical of a galaxy that is clearly composed of an ancient stellar population: it is the locus of old and intermediate-age RGB stars, low asymptotic giant branch (AGB) stars and blue-loop stars, some hundred million years old. A significant number of red bright stars are observed above the tips of the fiducial RGB ridgelines and they could be intermediate-age AGB stars covering a wide range of ages and metallicities. In addition, there is also an important population of young stars (age  $< 1$  Gyr): these include main sequence stars; core helium burning stars in the blue supergiant and/or in the blue loop region at  $V-I \lesssim 0.9$  (mag); and red super-giants at  $0.9 \lesssim V-I \lesssim 1.3$  (mag).

The CMDs in these different regions also display some marked differences in morphology that cannot be not fully explained by differences in observational effects. Most notably, the CMD of the innermost region appears stretched to red colours, mainly due to severe stellar crowding as judged by the completeness tests of the previous section. Incidentally, this crowding issue highlights the need for near-diffraction limited imaging at extremely large ( $> 20$  m class) optical/IR telescopes. In addition, there is an absence of stars at  $I < 22$  mag in field F2 that is not explained by incompleteness; the significance of this is discussed later in Sec. 5 and Sec. 6. Lastly, we see a dense string of stars at  $V-I \sim 0$  and  $I < 23$  mag in the F1 field that could well be the stellar main sequence; the finding is especially noteworthy because incompleteness would tend to suppress such features (see Fig. 4).

For a comparative analysis of the star counts in the fields at intermediate radii (F1 and

F3), we determined the ratio of star counts in three age-sensitive CMD boxes to the star counts in an RGB/old AGB box. The boxes are indicated in Fig. 4 and the associated star counts and ratios are given in Table 2. The data indicates that the F1 field has on average 3 - 4 times more stars, or similarly, that it is brighter by 1 - 1.5 magnitudes than the F3 field. We also find that there is a young population gradient in the F1 field, probably because it covers a possible spiral arm star forming region (Fig. 5). Lastly, unlike the old populations ( $> 1$  Gyr), there is a marked difference in the relative number of young stars in the two fields. In the outermost field (F4) there is a stark absence of bright stars ( $I \lesssim 24$  mag) with respect to the F1 field. As the surface brightness difference with respect to the F1 field is significant ( $\sim 2.7$  magnitudes) as measured by Carignan (1985), our observation of a dim disk field would be expected.

The expected number of foreground stars contaminating our CMD was estimated based on the Kim et al. (2002) study, galactic models, and the Hubble Deep Field to be about  $1 \pm 1$  and about 5 per pointing, at  $I < 17.5$  mag and  $I < 23$  mag respectively. The number of contaminating galaxies was estimated for several fields of the Medium Deep Survey (Griffiths et al. 1994) – and our selection criteria (stars brighter than  $I = 23$  mag) is expected to be robust against background galaxy contamination at these bright magnitudes, estimated to be  $1 \pm 1$  per WFPC2 pointing and thus an unlikely source of contamination which was not assessed by the artificial star test. The expected number of (unobscured) globular clusters in the WFPC2 fields based on Kim et al. (2002; hereafter referred to as K02) is at most  $1 \pm 1$ . Such objects would have V-I colours mostly in the range 0.9-2.0, and integrated I-band magnitudes of about 16-17 mag at the distance of NGC 300 based on the Milky Way globular cluster system (Harris 1996).<sup>4</sup>

---

<sup>4</sup>We have checked whether some of the candidate globular clusters from Kim et al. (2002) appear in the WFPC2 frames. One of them (their ID 8) occurs in the F1 field (chip 1) while

#### 4. TRGB distance to NGC 300

The most recent estimate of the distance to NGC 300 is by Freedman et al. (2001) using Cepheids. In the context of distance verification, it is important to verify this estimate using a different distance indicator. We have used the dereddened magnitude of the TRGB,  $I_{\text{o,TRGB}}$ , to derive the distance modulus of NGC 300 based on the widely used approach described by Lee, Freedman, & Madore (1993, hereafter LFM93), and typically has errors less than 10%. It has been assessed theoretically by Salaris & Cassisi (1998; hereafter SC98) who found that differences between TRGB and Cepheid distances are no correlated with metal content. Incidentally, it is the first such distance measurement for NGC 300. Distances to several other Sculptor Group galaxies have been measured previously using the same method (Karachentsev et al. 2003).

For the  $I_{\text{TRGB}}$  determination we consider the F1 and F3 fields, and ignore the remaining two fields due to a low number of stars and blending in the innermost field. To reduce the contribution of young/intermediate age stars, we selected stars with  $(V-I) > 1.5$  (mag). To measure the I-band magnitude of the TRGB, we applied the edge detection method described by Sakai, Freedman & Madore (1996). Firstly, for a sequence of magnitude values, we created a smoothed luminosity function,  $\Phi(m)$ , by replacing each magnitude value by a Gaussian distribution whose width (standard deviation) is the magnitude uncertainty (e.g. Fig. 6 (panel 3)). The edge-detection response is

$$\text{ED} = \Phi(m - \sigma_m^-) - \Phi(m + \sigma_m^-) \quad (1)$$

---

the other (ID 6) appears in the centre field (chip 1). However, both objects are saturated in the WFPC2 frames, and there are neighbouring stars, further study of them has not been pursued.

where  $\bar{\sigma}_m$  is the average  $\sigma_m$  at  $m \pm 0.05$  mag. ED was calculated at I-band magnitude steps of 0.01 mag. Next, we took 85% of these stars in a random way, and as a first estimate of the  $I_{\text{TRGB}}$  magnitude we recorded the magnitude at which the filter response is a maximum at  $I < 22.7$  mag. To determine the uncertainty in the tip magnitude, we performed a so-called bootstrap resampling of the data by repeating the procedure 500 times. We then fitted a Gaussian to a histogram of the tip magnitude estimates (binned at 0.01 mag). The peak magnitude from the Gaussian fit is taken as  $I_{\text{TRGB}}$  and the error in the Gaussian is taken as the uncertainty (Fig. 6, top). These values are given in Table 4. For the F3 field, the tip magnitude estimate is not reliable due to the low number of star counts, as is seen by the poor convergence of tip estimates (Fig. 7, top).

To determine how much these values depend on the fraction of stars selected, we varied the fraction selected from 0.6 to 0.9, and got the same  $I_{\text{TRGB}}$  value and only a slightly larger uncertainty. To test for a possible bias on the TRGB magnitude caused by incompleteness we multiplied the smoothed luminosity function by a monotonically decreasing function [1.0:0.80] in the magnitude range 22-24 mag and found no sensitivity to this. Another source of potential bias comes from smoothing the luminosity function. Cioni et al. (2000) reported the Sobel filter to be a biased estimator of the TRGB and that the bias depends on the amount of smoothing in the luminosity function at the location of the TRGB. To test our sensitivity to smoothing we varied the smoothing window in the range 0.04-0.06 mag and find negligible change in the mean tip magnitude and a slight change in errors.

The absolute I-band extinction,  $A_I$ , toward NGC 300 can be derived assuming the reddening law  $R_V = [A_V/E(B-V)] = 3.1$  and  $A_I/A_V = 0.48$  (Cardelli, Clayton & Mathias 1989). From the COBE/DIRBE and IRAS dust maps analysed by Schlegel, Finkbeiner, & Davis (1998; hereafter referred to as SFD98) we have  $E(B-V) = 0.013$  mag at its galactic coordinates ( $l = 299.21$  deg,  $b = -79.42$  deg from Simbad), which is similar to the 0.008 mag

from the lower resolution dust maps of Burstein & Heiles (1982; hereafter referred to as BH82). Adopting the SFD98 value, we get  $A_V = 0.039$  mag, and  $A_I = 0.019$  mag. The values are included in the dereddened I-band magnitude of the TRGB in Table 4. The possible presence of significant amounts of dust in the observed fields is a concern that is explored in more detail in Sec. 5.

Next, we calculate  $M_{I,TRGB}$ , using three methods for comparative reasons. In the first method we adopt the value  $M_{I,TRGB} = -4.06 \pm 0.07$  (random)  $\pm 0.13$  (systematic) mag from Ferrarese et al. (2000; hereafter referred to as F00). They treated the TRGB as a secondary distance indicator and calibrated a zero point from galaxies with Cepheid distances. The calculated distance modulus,  $(m-M)_o$  is, therefore,  $26.56 \pm 0.07$  (random)  $\pm 0.13$  (systematic) mag. Importantly, it is in good agreement with the recent Cepheid-based estimate by Freedman et al. (2001). The caveat is that the present distance estimate is not strictly an independent empirical estimate.

The second method is the empirical, Cepheid-independent one suggested by Lee et al. (1993). Summarized by SC98 (their p 168), it is based on the relation between the (dereddened) I-band distance modulus and  $I_{o,TRGB}$ , i.e.  $(m - M)_o, I = I_{o,TRGB} + BC_I - M_{bol,TRGB}$ . The I-band bolometric correction,  $BC_I$ , is determined using

$$BC_I = [-0.881 - 0.243(V - I)_{o,TRGB}] \pm 0.057 \text{ mag} \quad (2)$$

from Da Costa & Armandroff (1990) where  $(V - I)_{o,TRGB}$  is the (dereddened) colour of the RGB locus at the tip magnitude.  $M_{bol,TRGB}$  is determined using

$$M_{bol,TRGB} = -0.19 \text{ [Fe/H]} - 3.81, \quad (3)$$

and [Fe/H] of the parent stellar population is related to the (dereddened) colour of the

RGB locus at  $M_I = -3.5$  mag ( $(V-I)_{o,-3.5}$ ) via

$$[\text{Fe}/\text{H}] = -12.64 + 12.6 (V - I)_{o,-3.5} - 3.3 (V - I)_{o,-3.5}^2 \quad (4)$$

both from Lee et al. (1993). With  $(V - I)_{o,\text{TRGB}} = 1.82 \pm 0.1$  mag<sup>5</sup> and  $(V-I)_{o,-3.5} = 1.58$  dex (field F1) we find  $[\text{Fe}/\text{H}] = -1.05$  dex and  $(m - M)_o = 26.62$  mag  $\pm 0.06$  (random; from  $I_{\text{TRGB}}$ ). This is in good agreement with the Cepheid-based calibration.

In the third method, we calculated  $M_{I,\text{TRGB}}$  using the theoretical calibration of SC98: the recipe makes use of their re-calibrated relation between the global metal-to-hydrogen ratio  $[\text{M}/\text{H}]$  and  $(V-I)_{o,-3.5}$ :

$$[\text{M}/\text{H}] = -39.270 + 64.687 [(V - I)_{o,-3.5}] - 36.351 [(V - I)_{o,-3.5}]^2 + 6.838 [(V - I)_{o,-3.5}]^3. \quad (5)$$

The SC98 recipe is based on updated stellar models, the empirical calibration of synthetic colours, and the adopted bolometric correction. They obtained the following relation for the absolute I-band magnitude of the TRGB:

$$M_{I,\text{TRGB}} = -3.953 + 0.437 [\text{M}/\text{H}] + 0.147 [\text{M}/\text{H}]^2 \quad (6)$$

which leads to  $[\text{M}/\text{H}] = -0.85$  dex, and  $(m - M)_o = 26.73 \pm 0.06$  mag (random). The difference between this value and the value from the Cepheid calibration (i.e. 26.56 mag; Freedman et al. 2001) is 0.17 mag.

The good agreement of the first method (empirical TRGB calibration of the distance tied to the Cepheid scale; F00), with Cepheid distance itself is not surprising. The TRGB

---

<sup>5</sup>Colour values were derived in a bootstrap way: 85% of the stars were randomly selected in an I-band interval of 0.1 mag (i.e.  $[I_{\text{TRGB}} : I_{\text{TRGB}} + 0.1 \text{ mag}]$  in the case of the RGB tip); and we then repeated this 500 times in order to obtain the average estimate with the standard deviation of the fit to the peak of the resultant data (binned at 0.05 mag) taken as the uncertainty.

distance from the Lee et al. (1993) calibration is an independent measure of the distance to NGC 300 and is in good agreement with the F00 measurement. There is, however, a discrepancy with the theoretical calibration of SC98, which may be a zero-point problem.<sup>6</sup> In conclusion, we adopt the F00 value of  $M_{I,\text{TRGB}}$  because it is precise and most especially because it is a statistically averaged solution whose zero-point derivation is based on a homogeneous and consistent calibration. The corresponding distance modulus estimate is given in Table 4.

## 5. Internal Extinction in NGC 300

For our study of the bright stellar populations of NGC 300, it is very important to consider the issue of internal reddening of the galaxy because it can broaden CMD features: internal extinction may vary locally depending on the spatial distribution of dust and stars (e.g. Jansen et al. 1994). It is probably low on average based on the dust maps of SFD98, which are in fact in good agreement with the values from the lower resolution dust maps of BH82 as mentioned in the previous section. Going one step further, we looked for a difference in extinction between the F1 and F3 fields. From the previous section, we know that the TRGB magnitudes in these fields appear not to differ by more than about 0.1 mag at most, which argues against significant differential extinction in these fields. This is especially meaningful because the I-band TRGB magnitude is fairly insensitive to variations in heavy element content (Salaris, Cassisi, & Weiss 2002), something that could partially mimic differential extinction.

---

<sup>6</sup>However, in support of the F00 calibration, we note that that a recent RR Lyrae star calibration of the LMC distance modulus by Clementini et al., (2003) gave  $18.515 \pm 0.085$  mag which is in good agreement with the value (18.50 mag) adopted by F00.

Another issue is extinction in the nuclear region of NGC 300. Indeed, although NGC 300 is near face-on, as opposed to edge-on in which central extinction tends to be higher, there is the possibility of significant extinction in the central region (Peletier et al. 1995). In contrast to the outer fields, there are clear shells of dust in the central region based on visual inspection of the ESO/WFI (real-) three-colour image <sup>7</sup> (Fig. 1). These shells are distributed in a fragmented, ring-like structure of de-projected diameter  $\sim 1.2$  kpc ( $\sim 1'$ ), with an annular thickness of 0.2-0.4 kpc ( $\sim 10\text{-}20''$ ), based on visual inspection. The dust ring appears to be symmetric about the bright compact central object studied recently by Böker et al. (2002). Significantly, there is a stark absence of blue colours in the image which suggests that there may be significant extinction, possibly hiding evidence of recent star formation, and /or that there has been relatively little recent star formation in the nuclear and circum-nuclear region. For the central region, Davidge (1998) found evidence to support the idea of suppression of recent star formation, a plausible result because the study was based on essentially extinction-free near-IR imaging.

Lastly, we remark that almost no reddening has been reported for two early-type super-giants, one near the galaxy centre (at  $r \sim 0.55'$ ) and one in the outskirts (at  $r \sim 9.16'$ ) (Urbaneja et al. 2002). However, it is very difficult to make specific conclusions regarding field-to-field differences in extinction from such a sparse sample and a larger sample is needed in order to place wide-field spectroscopy-based reddening information on a firm statistical footing.

---

<sup>7</sup>A high resolution colour image is included in the online electronic version

## 6. The Young Stellar Population

We checked whether there are any spatially distinct stellar groups or associations of stars younger than about 1 Gyr in the F1 and F3 fields at  $I < 24$  (mag) (i.e. an extension of box A in Fig. 4). For this, a histogram of the number density of stars in 100 pixel wide columns was then computed. In each histogram, a background and  $4\sigma$  detection threshold level was determined from the first 750 columns of the WFPC2 frame. In this way, any detection is neither affected by the WFPC2 L-shape, shown in Fig. 5, nor statistical fluctuations. While there is no real evidence for a stellar group in the F3 field, there is a significant group in the the other field (F1). For validation of the detection, we varied bin size from 50 to 150 pixels; and the significance remains. Based on a Gaussian fit to the histogram for field F1, we find the size (FWHM) to be about 140 pc, at a distance of  $2.02 \pm 0.07$  Mpc (e.g. Freedman et al. 2001). This is consistent with the average OB association size in NGC 300 (Pietryński et al. 2001). Based on the work of Kim et al. (2002) who age-dated 15% of the 117 OB associations cataloged by Pietryński et al. (2001), the age of the newly detected association would be of the order of 10 Myr or less, and is approximately of average size. Accordingly, bright main sequence and/or blue supergiant stars may be present. We note that none of the X-ray sources detected by the ROSAT HRI (Read et al. 2001) occur in the F1 field, or the other fields. The coordinates of the association are given in Table 3.

Another issue is star forming environments. The F1 field covers parts of a major and minor spiral arm (see Fig. 1 and Fig. 5 (bottom)). The blueness of these arms with respect to the interarm region argues for a rich supply of young stars at the southern end of the F1 field which is also indicated by Fig. 5 (top). Consequently, it is not suprising that there are parts of OB associations cataloged by Pietrynski et al. (2001), namely AS 054 and AS 055, at the southern end of the WFPC2 FoV (Fig. 5). We note that of the Wolf-Rayet

stars found by the Schild et al. (2003) survey of several fields and the associations of OB stars cataloged by Pietryński et al. (2001), a few such stars occur in our fields, but did not meet our selection criteria (see Sec. 2: i.e. rejected as saturated; stellar blends; and or large fitting/photometry errors) and have been ignored.

Pursuing the SF issue further, we refer to cataloged blue stars, OB associations, and the correlation made with  $H_{II}$  maps by Pietryński et al. (2001). From their Fig. 4 we see that there is a significant drop-off in the number of OB associations at  $r \sim 9-12'$  (projected). Consequently, if these were used as tracers of star formation, one would conclude that such activity is significantly lower at large radii with respect to that of the disk. We also note that there are some blue stars at  $r = 12-13.5'$  that might be tracing the galaxy out to even larger radii, or possibly associated with parts of tidal streams; but we cannot exclude the possibility that such stars are simply just the bright field star population that one expects (see Sec. 7).

The next issue is the amount of recent star formation. Based on the presence of blue helium burning stars in Fig. 8, a marked recent burst of star formation in the observed fields is likely. However, the small WFPC2 field of view certainly means that the brightest population of stars may not have been sampled adequately. Nevertheless, we can say that star formation may well be continuing at the observed pointing, statistically speaking, based on the presence of a blue plume stretching up to  $V \sim 18$  mag ( $I \sim 18$  mag also) in the (V,B-V) CMD of Pietryński et al. (2001) which covers the whole galaxy. Such stars may be in OB associations, or less concentrated star forming regions. Guided by the isochrones in the same figure, we also see clues there may have been very recent star formation because of some bright, possibly zero-age main sequence stars at  $V-I \sim 0.4$  mag that are present.

Lastly, there is evidence for a difference in the stellar content of the field F1 and F3. One can see that there is a relative dearth of intermediate mass stars in the range  $5-12 M_{\odot}$

in the F3 field with respect to the F1 field: such stars in the F1 field are predominantly associated with the spiral arms (see Fig. 5). We recall from Sec. 3 that the ratio of old to young ( $\lesssim 1$  Gyr) stars for the two fields are not in good agreement (see Table 2), and so the observation cannot be attributed completely to the difference in surface brightness (or the mean star formation activity) between two disk fields (see Sec. 3). It can be attributed to the significant difference in the star formation rate at these locations in NGC 300 as shown in Sec. 8 and Fig. 10.

## 7. Star Formation History

In each of the two fields at intermediate radii (F1 and F3) one finds that only the brightest stars have been detected. Accordingly, the associated CMDs do not permit a detailed derivation of the star formation history (SFH) using synthetic CMDs. Despite this, we may broadly estimate how the heavy element abundances and star formation rate (SFR) has changed during the lifetime of NGC 300. We have followed the method and have adopted the hypotheses introduced by Aparicio et al. (1997) and Martínez-Delgado, Aparicio & Gallart (1999). We refer to these papers for a detailed description of the method. However, a brief summary here is appropriate.

In short, the SFH is considered to be composed of three functions: the SFR,  $\psi(t)$ ; the Initial Mass Function (IMF); and the chemical enrichment law,  $Z(t)$ . With these functions as input, the synthetic CMDs were computed using scripts introduced by Aparicio et al. (1997). For the analysis, we have assumed a Salpeter IMF (Salpeter 1955) with low and high mass cut-offs at  $0.7 M_{\odot}$  and  $30 M_{\odot}$  respectively, and have ignored the possible effects of binary stars because the old population in our CMD is mainly composed by RGB and AGB stars. Such stars are expected to be well-mixed in the disk by the present time: with a random velocity of  $1 \text{ km s}^{-1}$ , the crossing time for a  $1.5 \text{ kpc}$  region or the WFPC2 field

size would be about 1.5 Gyr. Consequently,  $Z(t)$  and the SFR have been determined for each WFPC2 field rather than for the individual chips in order to maximize signal-to-noise.

For determination of  $Z(t)$ , we considered six age intervals with widths suited to the present use of V-, and I-band photometry, which is anyway relatively insensitive to variations in  $Z(t)$ . These intervals are: 15 to 12 Gyr, 12 to 9 Gyr, 9 to 6 Gyr, 6 to 3 Gyr, 3 to 1 Gyr. For each age interval, we adopted a constant SFR, and synthesized a stellar population of 40,000 stars with absolute magnitudes brighter than  $M_I = -3.0$  mag. The chemical abundance ( $Z$ ) of each star has been taken at random. Internal photometric errors from the artificial star tests described in Sec. 2 have been included.

In order to estimate the mean heavy element ( $Z$ ) abundances of each age interval, we adopted the following recipe. Firstly, we selected stars from the synthesized population of stars with heavy element abundances in an arbitrary range ( $Z_1$  to  $Z_2$ ). Then we measured the position and full width of the synthetic RGB/AGB locus for stars at  $22.55 < I$  (mag)  $< 26$  and  $V-I > 1.4$  mag. This procedure was repeated a few hundred times for different  $Z$  ranges. From the resultant database, only those  $Z$  pairs giving synthetic colours and widths that closely matched the values from the real CMD data were chosen. In this way we could obtain an estimate of the maximum and minimum  $Z$  values in each age interval that are consistent with the real CMD data. The two  $Z$  indicators (width and position of the RGB/AGB locus), however, sometimes returned different  $Z$  pairs: the standard deviation of the differences is taken as an estimate of the uncertainty in  $Z(t)$  which is plotted in Fig. 9. For a test of the robustness of this  $Z(t)$  solution to the selected CMD area, defined above, we varied the I-band range and colour boundary by up to 0.1 mag. The variation in  $Z$  is of the order of 20% which is consistent with the largest error bar size.

For the past 1 Gyr, our only estimate of the mean  $Z$  abundance comes from spectroscopy of two blue super-giants outside the central region ( $r \gtrsim 2.3'$ ) of NGC 300 (Bresolin et al.

2002b, Urbaneja et al. 2002)<sup>8</sup>. We take the average and rms of these, and included them in Fig. 9. It turns out that extrapolation of  $Z(t)$  to ages less than 1 Gyr leads to a fine agreement with the empirical estimates; but ongoing (e.g. Bresolin et al. 2002b) and future spectroscopic studies are needed for better global  $Z$  information on NGC 300.

Next, we computed a synthetic CMD for a stellar population with ages in a narrow interval using a library of stellar evolution tracks (Bertelli et al. 1994). We call this a partial CMD: taking a set of partial CMDs, each covering different age intervals (e.g. several times  $10^8$  yr to a few times  $10^9$  yr), the full galaxy age ( $\sim 15$  Gyr) is accounted for. A combination of partial CMDs that covers the full age of the galaxy is called a candidate global synthetic CMD.

For each real CMD, we computed a total of 50,000 candidate global synthetic CMDs in the following way. Each such CMD was made by simply extracting all stars from the synthesized stellar population (mentioned earlier) such that in each age interval<sup>9</sup> there are only stars of the right age and each star has a synthesized  $Z$  value between the estimated maximum and minimum value for that age interval. In the next step, we selected eleven relatively age-sensitive CMD boxes sampling the main features of the real CMD; and counted the stars in those boxes (see Fig. 4). To paraphrase Aparicio et al. (1997), let us label the number of stars in box  $j$  of the observed CMD with  $N_j^o$ , and the number of stars

---

<sup>8</sup>The CMD may not be used mainly due to the lack of a relatively  $Z$  sensitive feature for stellar ages below about 1 Gyr – e.g. Fig. 8, right-hand panel

<sup>9</sup>Shorter age intervals were adopted for the past 6 Gyr than for the  $Z(t)$  estimate (see Fig. 10) because time resolution is potentially much better for SFR calculations than that of  $Z$  over the past few  $\times 10^9$  yr, especially if dramatic SFR changes could have occurred (e.g. see Williams 2002). Interpolation was used to assign minimum and maximum  $Z$  values to the shorter age bins at ages greater than 1 Gyr.

in box  $j$  of the partial CMD  $i$  with  $N_{ji}^m$  (the partial CMD of the  $i^{\text{th}}$  age interval).  $m$  is the total number of candidate synthetic CMDs generated. The star counts per box are related to each other by

$$N_j^m = k \sum_i \alpha_i N_{ji}^m \quad (7)$$

where  $\alpha_i$  is the linear combination coefficient in age interval  $i$ , and  $k$  is a constant scaling factor.  $\alpha_i$  and  $k$  are related to the SFR,  $\psi(t)$ , by:

$$\psi(t) = k \sum_i \alpha_i \psi_i \Delta_i(t) \quad (8)$$

where  $\Delta_i(t) = 1$  if  $t$  is inside the current age interval of interest (corresponding to the partial model  $i$ ; or similarly, the model associated with the age interval  $i$ ), and  $\Delta_i(t) = 0$  otherwise (Aparicio et al. 2001); and  $\psi_i$  corresponds to partial model  $i$ . The  $\psi(t)$  values having the highest probability of fitting the data in a chi-squared<sup>10</sup> sense can be obtained by a least-squares fitting of  $N_j^m$  (i.e. simulated star counts) to  $N_j^o$  (i.e. observed or real star counts), where the  $\alpha_i$  coefficients are the free parameters and each is chosen randomly in the range 0 to 1. Coefficients that provide synthetic CMDs that best match the real CMD will have the smallest  $\chi^2$  values. Accordingly, after producing 50,000 sets of coefficients (i.e. 50,000 candidate SFR solutions<sup>11</sup>), one has a distribution of  $\chi^2$  values. The wide spread actually occurs because there are no unique age indicators for each age interval in our CMDs: indeed, none are expected because of the large degeneracy between age and

---

<sup>10</sup> $\chi^2 = \sum_k ((N_j^o - N_j^{\text{fit}}) / N_j^o)^2$  where  $k$  is the number of candidate solutions.

<sup>11</sup>The common SFR zero point is determined by knowing the total initial stellar mass of all stars generated while producing the synthesized stellar population.

chemical composition in our data<sup>12</sup>. Thus, we take the standard approach of taking the average of the best solutions with their standard deviation representing the uncertainty: here, we define the best solutions as those meeting a  $\chi^2$  cut-off criterion. This criterion is taken as  $\chi^2 < (\bar{\chi}^2 - 3\sigma)$ , where  $\sigma$  is the standard deviation in the  $\chi^2$  distribution. With this, a few hundred SFR solutions or less than 1% of all the candidate solutions were selected. For each set of coefficients that satisfied the criterion, an estimate of the SFR(t) was obtained; and the standard deviation of all the SFR estimates in a given time interval was taken as the uncertainty in that interval. The mean SFR is plotted on a logarithmic scale against time in Fig. 10 for each field together with the estimated SFR uncertainty.

In order to test the robustness of the derived SFR trend, we also used a different cut-off, namely the  $\bar{\chi}^2 - 2\sigma$ , giving about 1700 global solutions, and has the effect of increasing SFR error bars only slightly and has a negligible change on SFR(t). We note that the typical error bar size indicates an uncertainty of about two to three in SFR in general, consistent with the uncertainties presented in studies that considered the upper RGB data and several age intervals between 15 Gyr and now (e.g. Aparicio et al. (1997), their Fig. 8 – LGS 3; Dolphin (2002), his Fig. 7, panel e – simulated galaxy with a relatively complex SFH). It is evident that error size in Fig. 10 tends to grow towards younger ages: on one hand this is due to the decreasing number of recently formed stars in the observed fields – which forces the use of wide age intervals for signal-to-noise reasons, while on the other hand there might well have been episodic star formation during the past few  $\times 10^9$  yr to

---

<sup>12</sup>Such degeneracy would be partially broken by a longer colour baseline than V-I, e.g. by including suitable near-infrared data. Importantly, however, star formation histories can be measured accurately when photometry reaches to  $M_V = +2$  mag (Dolphin 2002), or fainter still, to ancient main sequence turn-off stars.

which our age binning is possibly fairly insensitive<sup>13</sup>.

Another point concerns the ability to estimate both  $Z(t)$  and  $SFH(t)$  from RGB and AGB star data alone, as opposed to also having data on horizontal branch and fainter structure. The concern stems from the difficulty of disentangling the contribution of age and chemical composition to stellar colour, the so-called degeneracy between the two parameters. Thus, in such a situation solving simultaneously for the true  $Z(t)$  and  $SFR(t)$  is difficult, even if possible, as the reasoning is flawed. The approach that we have applied is, however, one solution to this problem. We recall that the approach that we have adopted has been to first assume a constant SFH and then to solve for  $Z(t)$ . Then this  $Z(t)$  has then been used as input in the effort to obtain the solution for the  $SFR(t)$ . Given the uncertainties in the final  $Z(t)$  and  $SFH(t)$ , the approach we have followed is deemed to be tolerable.

Even though a detailed chronology of star formation in the WFPC2 field over the past few  $\times 10^9$  yr is beyond the scope of the present paper, we can form broadly acceptable conclusions on SF activity. Discussion of this issue is given in Sec. 8.

In order to test the reliability of the derived star formation history, we present the synthetic CMDs derived for the fields (F1 and F3) for which an SFH analysis has been possible (Fig. 11), for comparison with the real CMDs (see Fig. 8); photometry uncertainties in the real data have been simulated and added. Overall, there is good agreement for each synthetic/observed CMD pair. The main difference is in the colour–magnitude spread: synthetic CMDs are inclined to have tighter features than their counterparts in the real astronomical data. This could be due to a range of extinction values for the stars (Williams

---

<sup>13</sup>Dolphin (2002; his Figs. 5 and 7) demonstrates this latter point through estimations of the star formation histories of synthetic galaxies with episodic star formation histories.

2002) that has not been estimated by the stellar population synthesis models. We note the difference in the star count density at red colours  $V-I \gtrsim 3$  mag at/near the RGB peak magnitude in the F1 field, for which the effect is pronounced, is not unexpected because incompleteness becomes significant for such stars. Additionally, the required completeness correction increases significantly at faint magnitudes ( $I > 23$  mag) which causes significant scatter in the real data.

## 8. Discussion – Star Formation

In Sec. 7, we determined a low time resolution chemical enrichment law and  $SFR(t)$  for two disk fields in NGC 300. In this Section, we summarize briefly the key findings based on WFPC2 data that give insight on the SFH of NGC 300.

The metallicity has been measured in two disk fields to be more metal poor on average than 0.006 (or  $0.33 Z_{\odot}$ ) during the lifetime of NGC 300 and, based on the available evidence,  $Z(t)$  appears to have changed relatively little during that time. The present day value of  $Z$  may be of the order of 0.0035 to 0.0055 based on two empirical (spectroscopic) estimates from Urbaneja et al. (2003). Their best-fit oxygen abundance ( $12 + \log O/H$ ) estimates for two blue supergiants are 8.3 and 8.65 dex (their Table 1). We note that Pagel et al. (1979) measured oxygen abundances in six  $H_{II}$  regions in NGC 300. They found oxygen abundances approximately in the range 8.6 to 9 dex. It is encouraging that the oxygen abundances from the two spectroscopy studies roughly agree; this fact strengthens confidence in the derived values of  $Z$  in the present paper for the past few  $\times 10^9$  yr.

For the star formation rate in disk fields F1 and F3, a simple estimate has been made (Fig. 10): the derived mean SF rates are  $0.002$  and  $0.04 M_{\odot} \text{yr}^{-1}$  in the F3 and F1 fields respectively. We note that the apparent SFR increase at about 100-200 Myr may

not be real because of the estimated uncertainty – the occurrence of this feature could be reflecting a common systematic error for both field, possibly due to the small number statistics available for such young stars, that is not assessed by the  $\chi^2$ -squared tests. The mean SF densities,  $\bar{\Psi}/A$ , are  $3 \times 10^{-4} M_{\odot} \text{ yr}^{-1} \text{ kpc}^{-2}$  and  $6 \times 10^{-3} M_{\odot} \text{ yr}^{-1} \text{ kpc}^{-2}$  in the F3 and F1 fields respectively. These SF density values are consistent with expectations for spiral disks: the SFR density in spiral disks can be up to about  $0.1 M_{\odot} \text{ yr}^{-1} \text{ kpc}^{-2}$  in spiral disks and typical activity exhibits a steady state behaviour (Kennicutt 1998); SF in nearby spirals has, on average, a strong dependence on galaxy type, weak or no dependence on spiral structure or the presence of a bar, and moderate dependence on past interactions (Kennicutt 1998). It may well be that the average SF activity in the NGC 300 disk follows the typical trend in nearby spiral disks, but conclusive evidence will only be obtained from future observations covering more of the galaxy.

On the other hand, Davidge (1998) reported a suppression of recent star formation in the central region of NGC 300 based on near-IR observations. In our completeness-corrected I-band luminosity functions for stars younger than a few times  $10^8 \text{ yr}$  (at  $V-I < 0.6 \text{ mag}$ ), and brighter than the 50% completeness limits, we also find a significant cut-off in the central function with respect to the F1 and F3 fields (Fig. 12). However, as mentioned in Sec. 5, the central extinction is unknown and may be significant: from the ESO/WFI image there is evidence for distinct dust shells in part of the F1 FoV that are superimposed on a much more widely spread dust cloud. Consequently, internal extinction could possibly explain the truncation of the central I-band luminosity function: about one to two magnitudes of I-band extinction would be needed in order to dim the brightest object observed in the outer fields ( $I \sim 18 \text{ mag}$ ) to match the brightest stars in the central field (Fig. 3). Lastly, central ring-like gas (but also dust) structures are expected based on simulations of the detailed chemical and dynamical evolution of galaxies (e.g. Samland & Gerhard 2003).

Another issue is that there has been an increase in SFR over the last few Gyr in NGC 300. We know that the observed increase in SF activity in the F1 and F3 disk fields is not unprecedented in some spiral galaxy studies: some sites in M31 have SF rates indicating that sufficient gas may have been retained and/or acquired for continued or episodic star formation (Williams 2002; Williams 2003, based on the SFR measured in OB associations).

Finally, there is the issue of why there has been relatively little increase in  $Z$  over time in NGC 300 and why it appears not to have changed significantly over the lifetime of the galaxy. A possible solution is that metal-poor gas has been acquired by NGC 300. In the context of metal-poor gas acquisition through past encounters, we note that intergalactic gas and stars may be a partial signature of such encounters: a clustering of  $H_I$  clouds around NGC 300 and NGC 55 was found by Haynes & Roberts (1979) based on sensitive 21 cm observations; but uncertainty over group membership of clouds remains (Haynes & Roberts 1979). We also note that colour gradients and morphological studies of spiral galaxies can reveal clues about past mergers: no evidence for a colour gradient in NGC 300 was found by C85, and a detailed study of the morphology of NGC 300 (e.g. examining distorted isophotes hinted at in Fig. 1) remains to be tackled.

## 9. Conclusions

We have presented the first WFPC2 V, I photometry for the Sculptor Group late-type spiral galaxy NGC 300 in four fields ranging from the centre to the outer-edge. In particular, we have the following conclusions.

1. We have derived the first estimate of the star formation history in two disk fields. Our analysis indicates that stars were born at similar epochs and star formation activity possibly increased on average over time, but at different mean rates.

2. The main stellar population is predominantly old, consisting of RGB and AGB stars, based on a synthetic CMD analysis.  $Z$  is found to have been more metal poor than 0.006 (or  $0.33 Z_{\odot}$ ) with no evidence for significant change in the mean  $Z$  value over time in both disk fields.
3. In the circum-nuclear region, we find a dearth of bright stars relative to two disk fields that cannot be explained by observational effects. Taken at face value, this finding would agree with the Davidge (1998) report of suppressed star formation there during the past  $10^9$  yr; but the possibility of significant central I-band extinction (up to about 1-2 mag) remains.
4. We have also reported a newly detected a young star association (probably up to  $\sim 10$  Myr old) of about average size ( $\sim 140$  pc) in one of the disk fields that probably coincides with a star-forming region.
5. Lastly, the distance modulus has been determined using Ferrarese et al. (2000) Cepheid-based calibration the tip magnitude of the RGB to be  $(m-M)_0 = 26.56 \pm 0.07$  ( $\pm 0.13$ ) mag. This is in good agreement with the Cepheid distance to NGC 300 from Freedman et al. (2001). Incidentally, both values are in good agreement between with the TRGB distance estimated using the Lee et al. (1993) empirical calibration, which is Cepheid independent. There is, however, a discrepancy with the theoretical calibration of the RGB tip magnitude from SC98, which may be a zero-point problem. Accordingly, this means that the same difference in magnitude between the Cepheid distance and the theoretical calibration of the distance for NGC 300 exists for galaxies in the HST key project on the extragalactic distance scale.

A. Dolphin is thanked for help using HSTphot, as is A. Aparicio for useful comments on the population synthesis code. It is a pleasure to thank the anonymous referee for several

useful questions and comments. DB acknowledges the support of the European research and training network on Adaptive Optics for Extremely Large Telescopes under contract HPRN-CT-2000-00147.

## REFERENCES

Andredakis, Y., Peletier, R. F. & Balcells, M., 1995 MNRAS, 275, 874

Aparicio, A., Gallart, C., Bertelli, G., 1997, AJ, 114, 680

Baggett, S., et al., 2002, in HST WFPC2 Data Handbook, v. 4.0, ed. B. Mobasher, Baltimore, STScI

Beasley, M. A., Sharples, R. M., 2000, MNRAS, 311, 673

Bertelli, G., Bressan, A., Chiosi, C., Fagotto, F., Nasi, E., 1994, VizieR On-line Data Catalog: J/A+AS/106/275Cat

Böker, T., Laine, S., van der Marel, R. P., Sarzi, M., Rix, H-W., Ho, L. C., Shields, J. C., 2002, AJ, 123, 1389

Bresolin, F., Gieren, W., Kudritzki, R-P., Pietryński, G., Przybilla, N., 2002a, ApJ, 567, 277

Bresolin, F., Kudritzki, R-P., Najarro, F., Gieren, W., Pietrynski, G., 2002b, ApJ, 577, L107

Clementini, G., Gratton, R., Bragaglia, A., Carretta, E., Di Fabrizio, L., et al., 2003, AJ, 125, 1309

Da Costa, G. S., Armandroff, T. E., 1990, AJ, 100, 162

Davidge, T., 1998, ApJ, 497, 650

Deharveng, L., Caplan, J., Lequeux, J., Azzopardi, M., Breysacher, J., 1988, A&A, 73, 407

Dohm-Palmer, R. C., Skillman, E. D., Mateo, M., Saha, A., Dolphin, A., Tolstoy, E., Gallagher, J. S., Cole, A. A., 2002, AJ, 123, 813

Dolphin, A., 2000a, PASP, 112, 1383

Dolphin, A., 2000b, PASP, 112, 1397

Dolphin, A., 2000c, ApJ, 531, 804

Dolphin, A., 2002, MNRAS, 332, 91

Ferrarese, L., Mould, J. R., Kennicutt, R. C. Jr., Huchra, J., Ford, H. C., et al., 2000, ApJ, 529, 745

Freedman, W. L., Madore, B. F., Gibson, B. K., Ferrarese, L., Kelson, D. D., 2001, ApJ, 553, 47

Gratton R. G., Bragaglia, A., Carretta, E., Clementini, G., Desidera, S., et al., 2003, A&A, 408, 529

Griffith, R. E., Ratnatunga, K. U., Neuschaefer, L. W., Casertano, S., Im, M., Wyckoff, E. W., et al., 1994, ApJ, 437, 67

Harris, W. E. 1996, AJ, 112, 1487

Haynes, M. P., Roberts, M. S., 1977, ApJ, 227, 767

Holtzman, J., Burrows, C. J., Casertano, S., Hester, J. J., Trauger, J. T., et al., 1995, PASP, 107, 1065

Ibata, R., Michael, L., Geraint F., Stolte, A., ApJ, 547, 133

Jansen, R. A., Knapen, J. H., Beckman, J. E., Peletier, R. F., Hes, R. 1994, MNRAS, 270, 373

Karachentsev, I., Grebel, E. K., Sharina, M. E., et al., 2003, A&A, 404, 93

Kennicutt, R. C. Jr., 1998, ARA&A, 36, 189

Lawrie, D. G., Graham, J. A., 1983, BAAS, 01.10, AAS Meeting 163

Lee, M. G., Freedman, W. L., Madore, B. F., 1993, ApJ, 417, 553

Martínez-Delgado, D., Aparicio, A., 1997, ApJ, 480, 107

Martínez-Delgado, D., Aparicio, A., Gallart, C., 1999, AJ, 118, 2229

Méndez, B., Davis, M., Moustakas, J., Newman, J., Madore, B. F., Freedman, W. L., 2002, AJ, 124, 213

Pagel, B. E. J., 1979, MNRAS, 189, 95

Pannuti, T. G., Duric, N., Lacey, C. K., Goss, W. M., 2000, ApJ, 544, 780

Pietryński, G., Gieren, W., Fouqué P., & Pont, F., 2001, A&A, 371, 497

Pietryński, G., Gieren, W., Fouqué P., & Pont, F., 2002, AJ, 123, 789

Richer, H. B., Pritchett, C. J. and Crabtree, D. R., 1985, ApJ, 298, 240

Sakai, S., Madore, B. F., Freedman, W. L., 1996, ApJ, 461, 713

Salaris, M., Cassisi, and S., Weiss, A., 2002, PASP, 114, 375

Salaris, M., & Cassisi, S., 1998, MNRAS, 282, 166

Salpeter, E. E., 1955, ApJ, 121, 161

Samland, M., Gerhard, O. E, 2003, A&A, 399, 961

Schild, H., Crowther, P. A., Abbott, J. B., and Schmutz, W., 2003, A&A, 397, 859

Schlegel, D. J., Finkbeiner D. P. & Davis, M., 1998, ApJ, 500, 525

Tully, R. B., 1988, *Nearby Galaxies Catalogue*

Williams, B. F., 2002, MNRAS, 331, 293

Williams, B. F., 2003, MNRAS, 340, 143

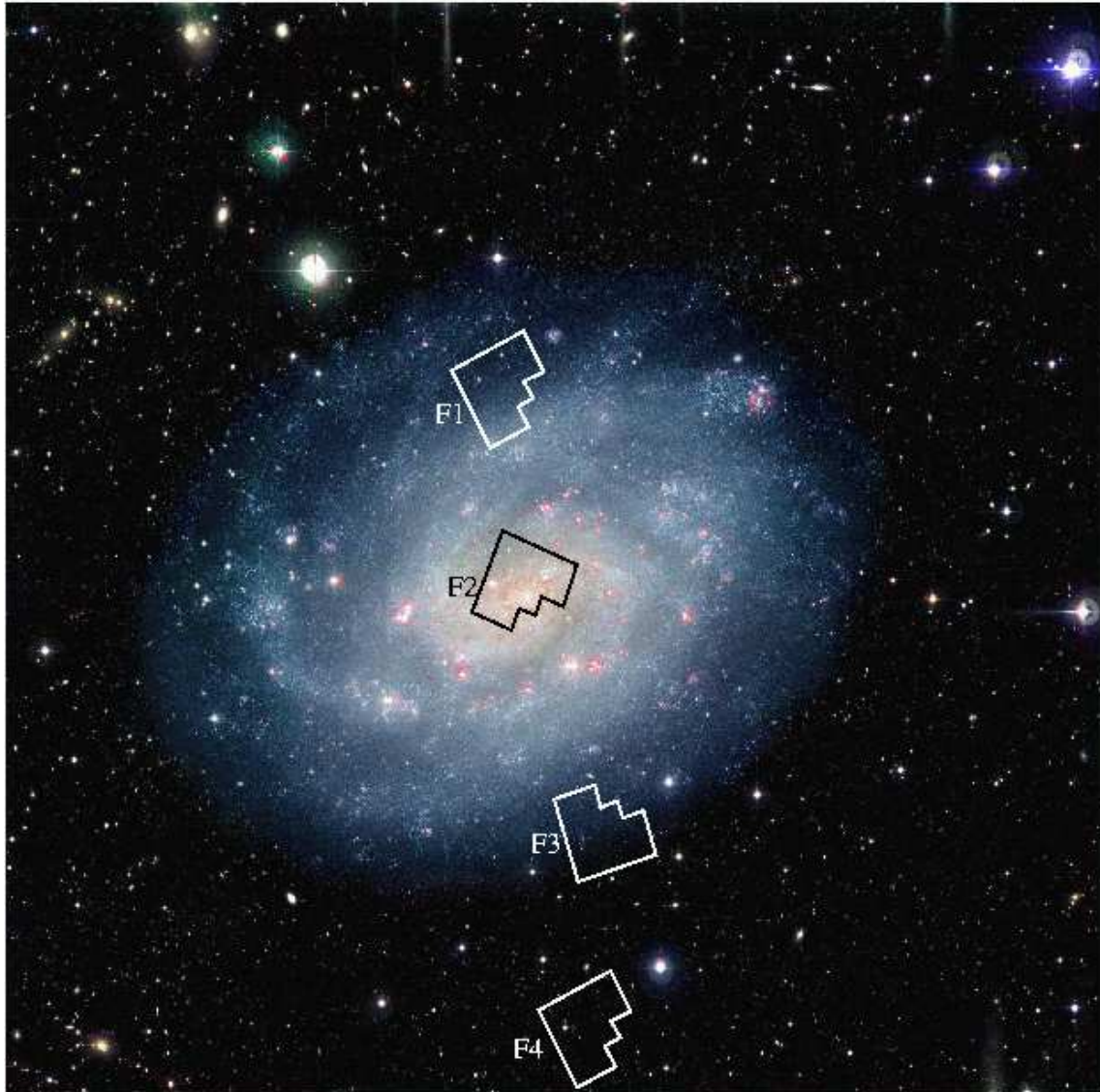


Fig. 1.— European Southern Observatory/Wide Field Imager (colour composite) image of NGC 300 with HST WFPC2 footprints superimposed. The field size is 34.6' square. WFPC2 positions:  $r = 5.99'$  (F1);  $0.44'$  (F2);  $7.12'$  (F3) ; and  $12.84'$  (F4). North is up and east is left.

Table 1. Source list: NGC 300 HST/WFPC2 archival data

Field	Radial distance <sup>a</sup> (arc min)	Radial distance <sup>b</sup> (kpc)	Date	Filter	Number of Frames	Integration Time (s)
F2	0.44	0.4	2001 May 06	F814W/F547M	2/4	300/400
F1	5.99	5.1	2001 July 02	F814W/F606W	2/2	300/300
F3	7.12	6.0	2001 Sept. 13	F814W/F555W	2/2	500/500
F4	12.84	10.9	2001 June 20	F814W/F606W	4/4	500/500

<sup>a</sup>Separations from cluster centre to the coordinates listed in the data pointings table (nominally the middle of the field of view) are taken from MAST, the multimission archive at STScI.

<sup>b</sup>De-projected radial distance in kpc based on an inclination of 46° (Tully 1988).

Table 2. Star counts in selected regions of the F1 and F3 CMDs.

Star counts	F1 (arc min)	F3 (arc min)
D: old AGB, RGB	646 (4.1%)	200 (7.5%)
C: old AGB	173 (8%)	49 (15%)
B: young AGB	74 (12.2%)	23 (22%)
A: < 1 Gyr	330 (5.8%)	68 (13%)
Count ratio		
C/D	0.27 (0.04)	0.24 (0.07)
B/D	0.12 (0.01)	0.12 (0.03)
A/D	0.51 (0.05)	0.34 (0.07)

The star counts (N) and ratios (corrected for a mean incompleteness of 10% at  $I < 23$  mag) come from defined CMD boxes (see Fig. 4). Star count error is  $\pm \sqrt{N}$ , determined for each uncorrected star count. Percentage error (top panel) and actual error (bottom panel) are given in parentheses. Box boundaries are defined in Fig. 4.

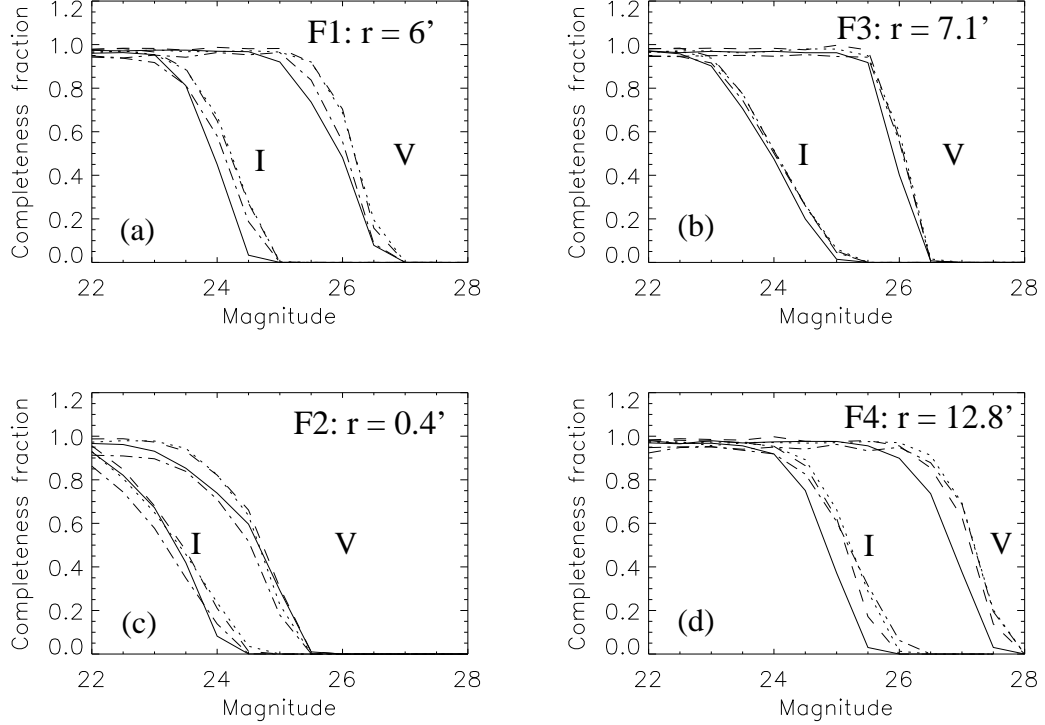


Fig. 2.— V, and I-band fractional completeness as a function of magnitude for WFPC-2 V-, and I-band PC1 (*solid*), WF2 (*dotted*), WF3 (*dashed*) and WF4 (*dot-dashed*) frames at each pointing as determined by artificial star tests. Completeness functions are the number of artificial stars recovered divided by the number of input stars; the bright ends of the functions in the above plots are typically less than 1.0 because of bad pixels.

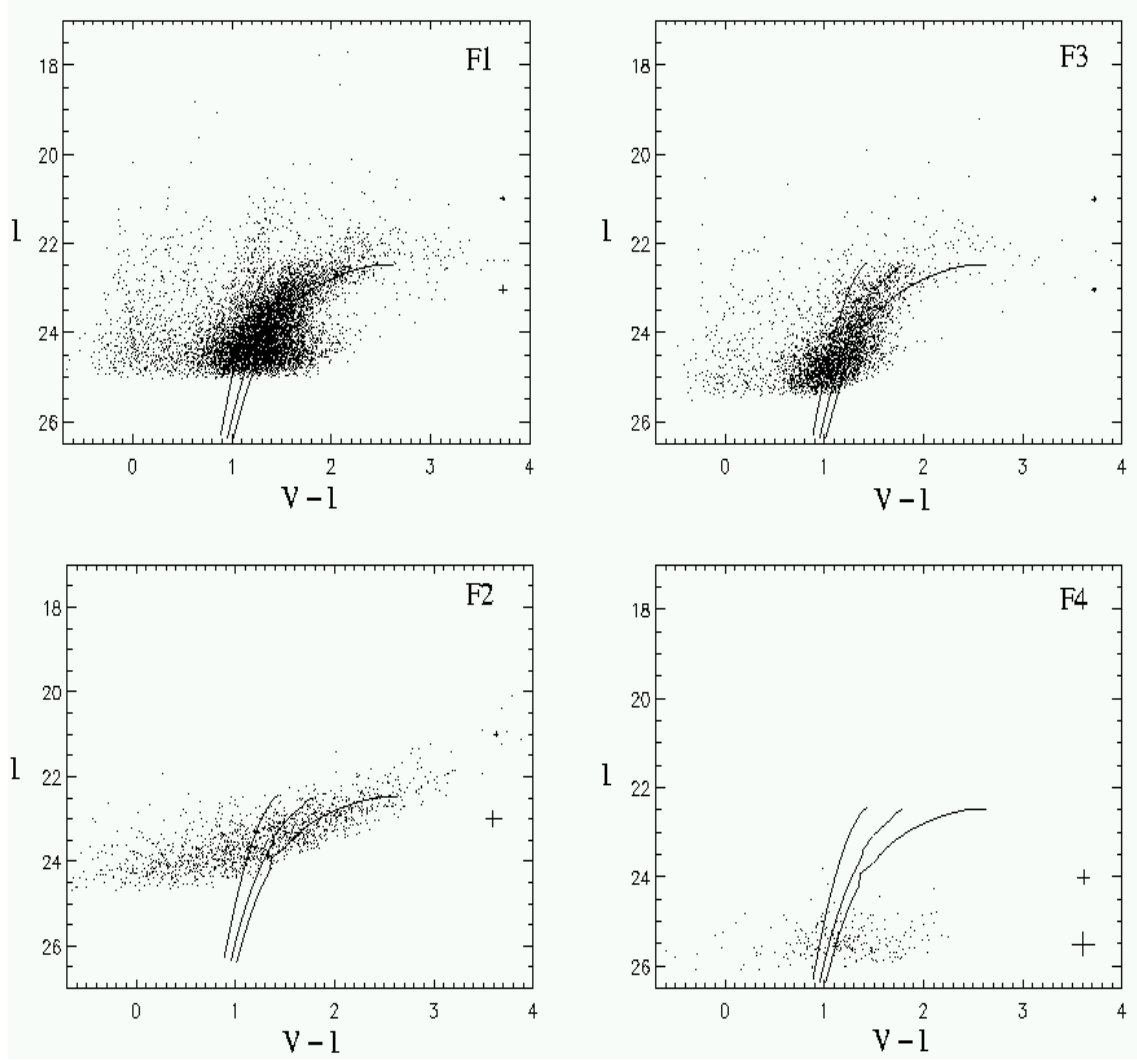


Fig. 3.— I, V-I CMD for four WFPC2 pointings in NGC 300. The plotted data consists of all stars with valid photometry (see Sec. 2). There are three globular cluster red giant branch fiducial ridgelines (*solid*), reddened using the  $A_V$  and  $A_I$  values given in Table 4. From metal-rich (right) to metal poor (left), they are for 47 Tuc,  $[Fe/H] = -0.71$ ; NGC 1851,  $[Fe/H] = -1.29$ ; and NGC 6397,  $[Fe/H] = -1.91$ . Included are photometry bars associated with  $V - I = 1$  mag.

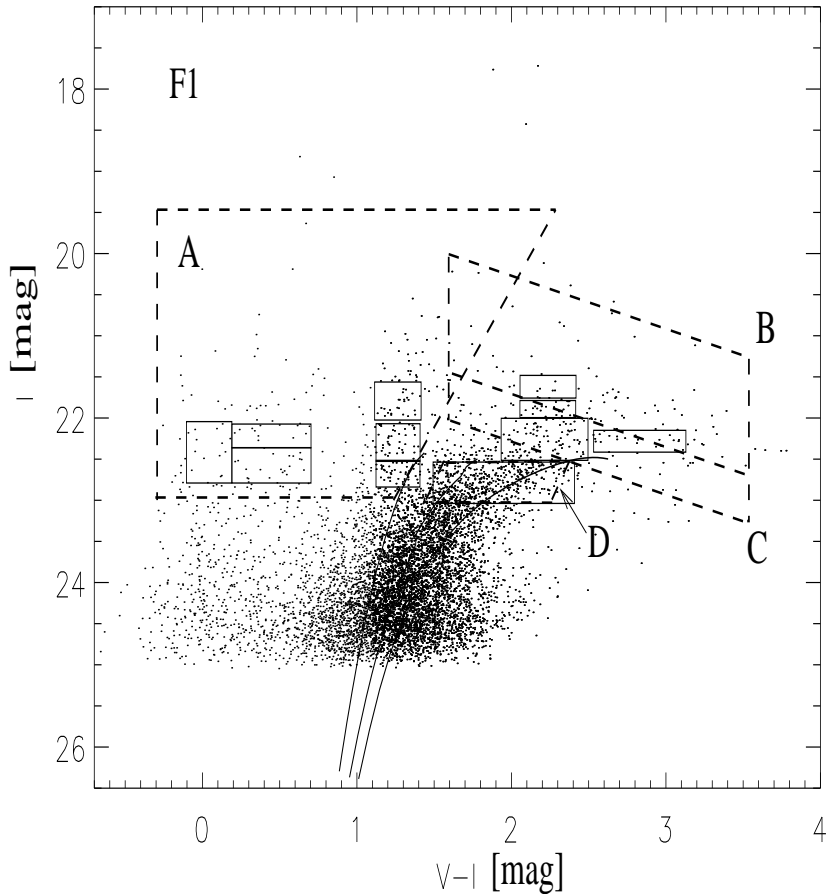


Fig. 4.— I, V-I CMD for field F1 including the four labeled regions used for the star count analysis in Sec. 3 (*dashed*). Also included are the eleven CMD boxes used to constrain the synthetic CMD (*solid*); see text in Sec. 7 for further details. The same boxes have been used for both the F1 and F3 fields. For the purpose of convenience, the stellar isochrones described in the caption of Fig. 8 are also included.

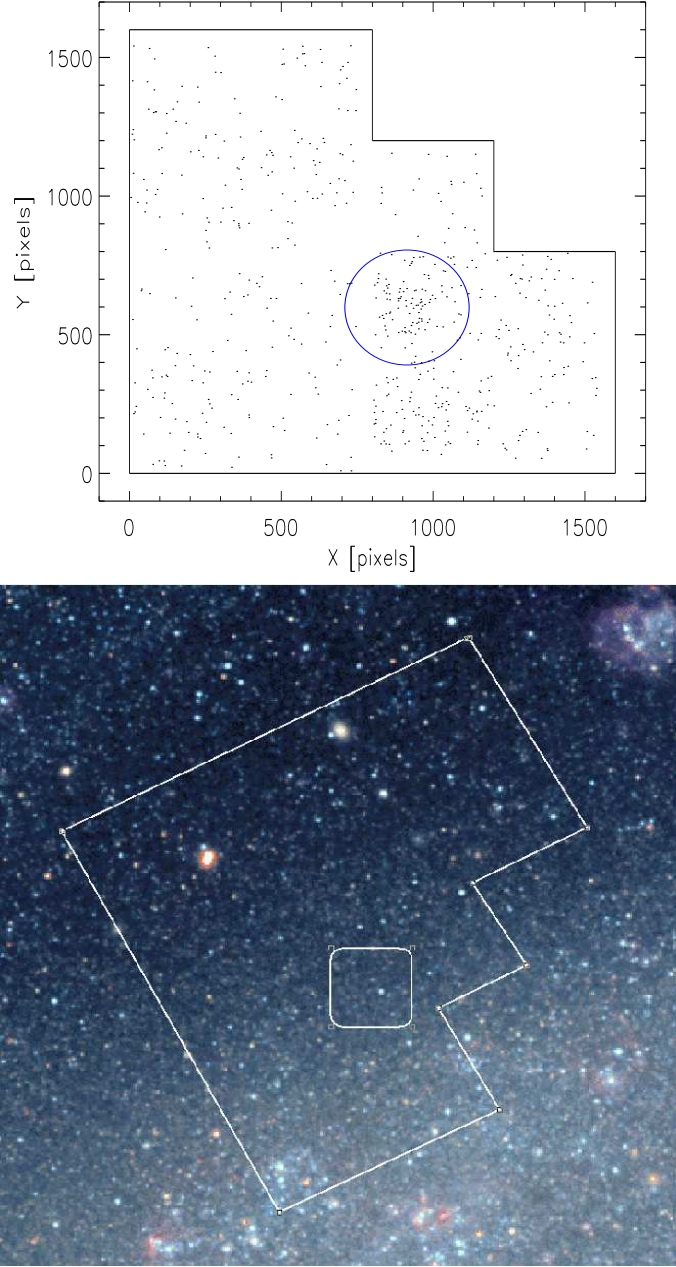


Fig. 5.— Star positions in the F1 field for stars younger than 1 Gyr (top) and section of the ESO/WFI image with the WFPC2 FoV overlaid. The discontinuity at columns 750 to 800 pixels (top) results from our setting their values to zero because of vignetting by the WFPC2 optics. In the ESO/WFI field, north is up and east is left. The small box indicates the approximate position of the newly detected stellar association. See text in Sec. 6 for further information.

Table 3. Coordinates<sup>a</sup> and size of newly detected stellar association.

$\alpha$ (J2000.0)	$\delta$ (J2000.0)	FWHM (pc)
00 54 56.6	- 37 35 25.0	130 - 145

<sup>a</sup>Units of right ascension are hours, minutes, and seconds, and units of declination are degrees, arcminutes, and arcseconds. Coordinates are taken from the online Aladin sky atlas: position error is estimated to be 10-20''.

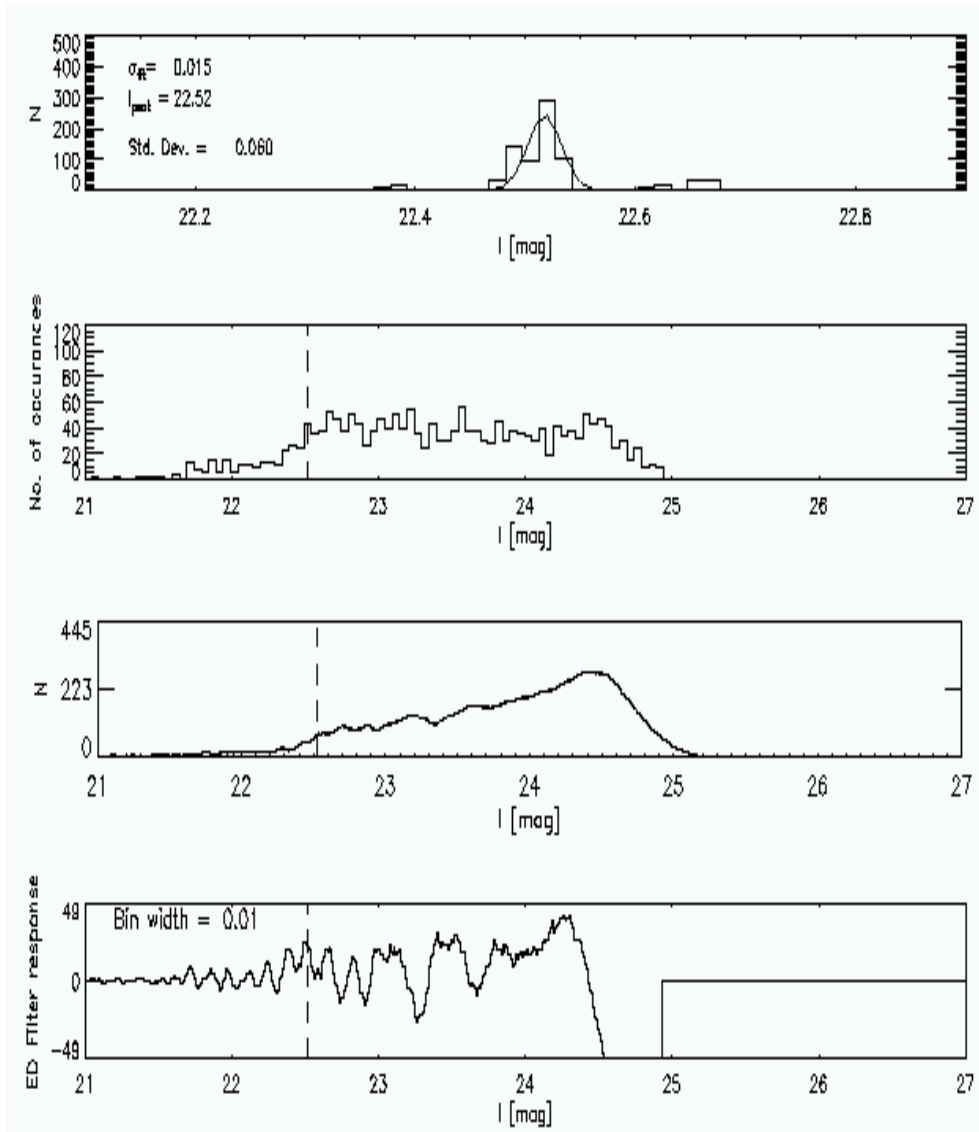


Fig. 6.— Deriving RGB tip magnitude in the F1 field. Top to bottom: Histogram of derived TRGB tip magnitudes, histogram version of the luminosity function, smoothed luminosity function, and an example edge detection filter response.

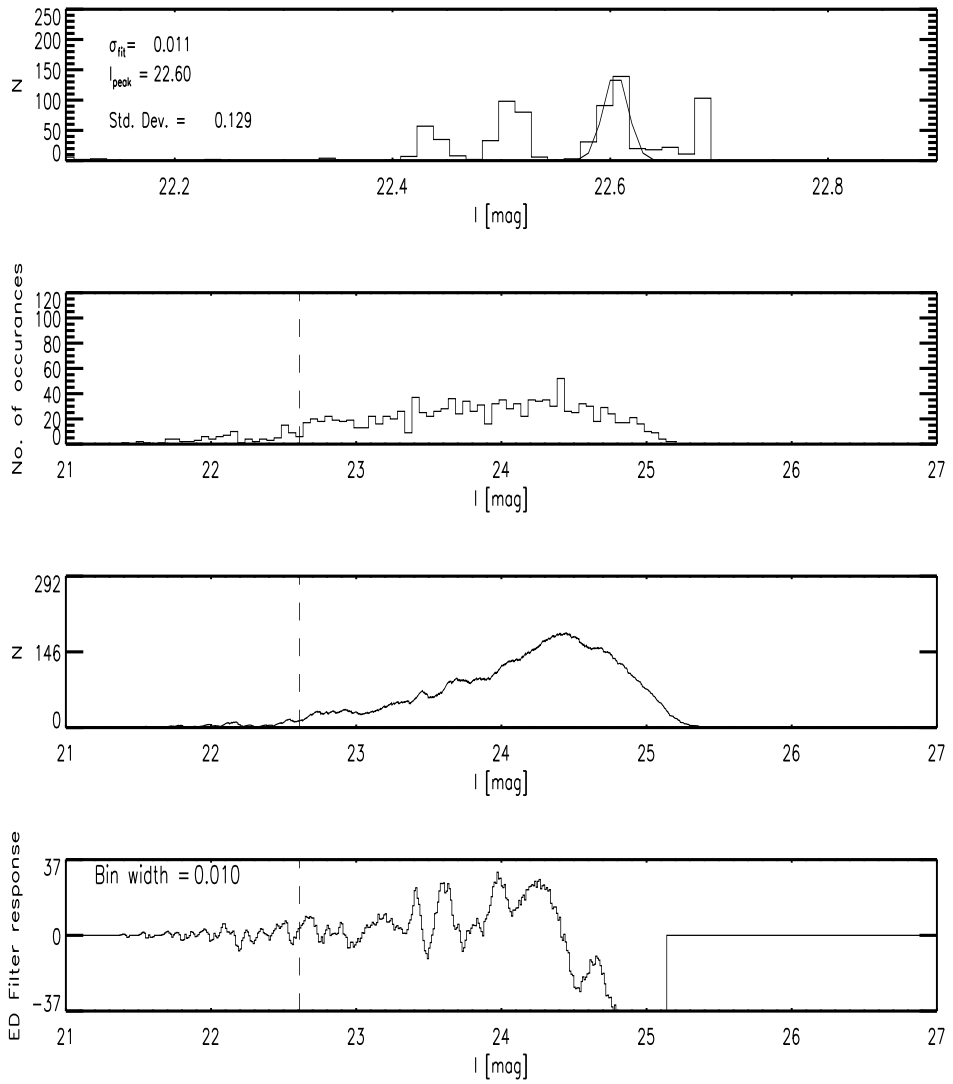


Fig. 7.— Deriving the RGB tip magnitude for the F3 field. Panels are as in Fig 6. Note that there is no clear unimodal-like distribution of bootstrap estimates in the top panel.

Table 4. Distance-related information for NGC 300.

Field	$I_{\text{TRGB}}$	$M_{I,\text{TRGB}} \pm r \pm s$	$A_V$	$A_I$	$(m-M)_0 \pm r \pm s$
(')	(mag)	(mag)	(mag)	(mag)	
(1)	(2)	(3)	(4)	(5)	(6)
F1	$22.52 \pm 0.02$	$-4.06 \pm 0.07 \pm 0.13^a$	0.039	0.019	$26.56 \pm 0.07 \pm 0.13$

<sup>a</sup>Ferrarese et al. (2000), with  $r$  = random and  $s$  = systematic.

<sup>b</sup>Taking median value, as a Gaussian fit is not possible; Columns (1) Radial distance of WFPC2 field from galaxy centre; (2) Tip I-band magnitude of the RGB. (3) Absolute I-band magnitude of the RGB tip; (4) and (5) Galactic foreground extinction (Schlegel, Finkbeiner, & Davies 1998) converted to I-band using the Cardelli, Clayton, & Mathis (1989) extinction law, and  $R_V = 3.1$  (NED); (6) distance modulus

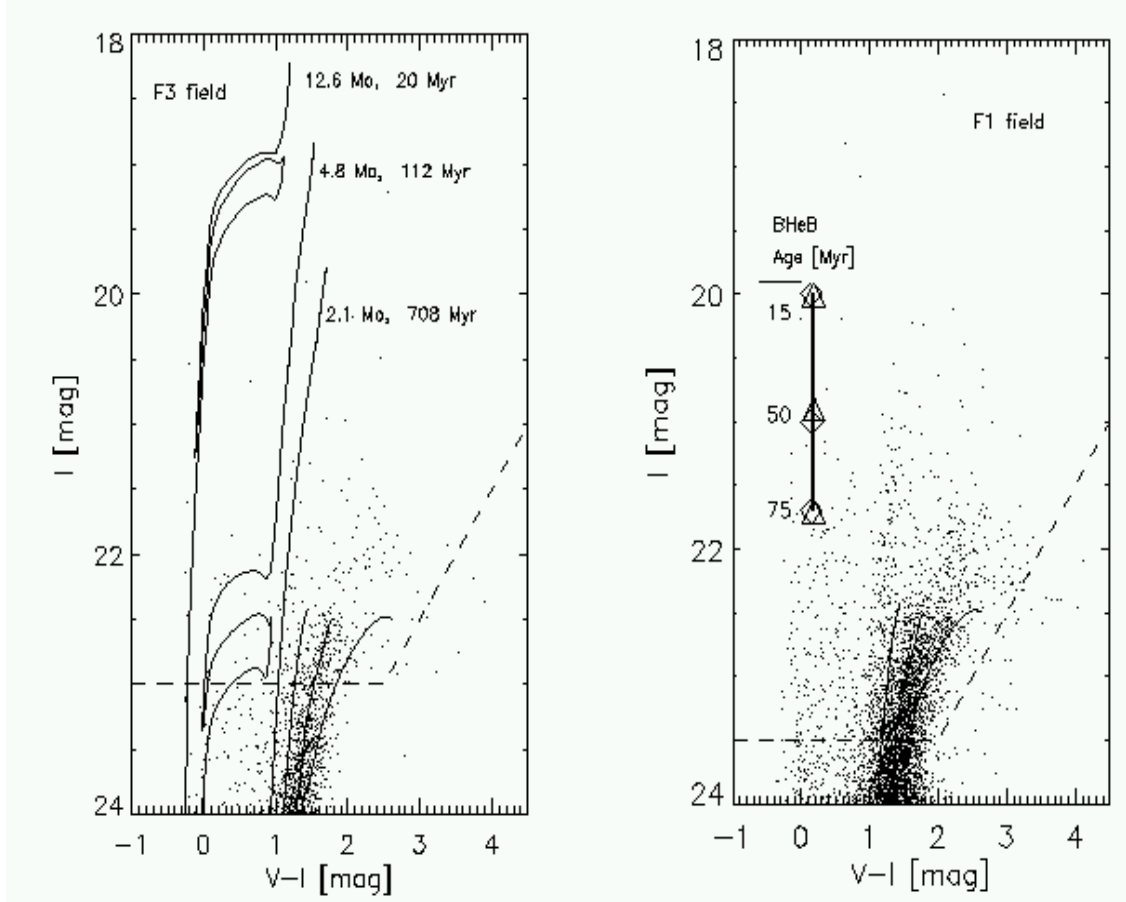


Fig. 8.— CMD for NGC 300 F1 and F3 fields. The stellar evolution tracks/isochores for the adopted  $Z = 0.004$  Padova models (see text) are plotted (*thin/solid*) in the left panel. These are labelled with the starting mass in solar units, and corresponding ages. The age – I-band magnitude trend for blue supergiant/core helium burning stars is marked in the right-hand panel for two metallicities, namely  $Z = 0.003$  (diamonds) and  $Z = 0.005$  (triangles); and age error sizes are smaller than the symbol sizes. From metal-rich (right) to metal poor (left), reddened ridgelines (*thick/solid*) are for 47 Tuc,  $[\text{Fe}/\text{H}] = -0.71$ ; NGC 1851,  $[\text{Fe}/\text{H}] = -1.29$ ; NGC 6397,  $[\text{Fe}/\text{H}] = -1.91$ . The adopted true distance modulus is 26.5 mag. The 90% completeness limit is also indicated (*dashed*).

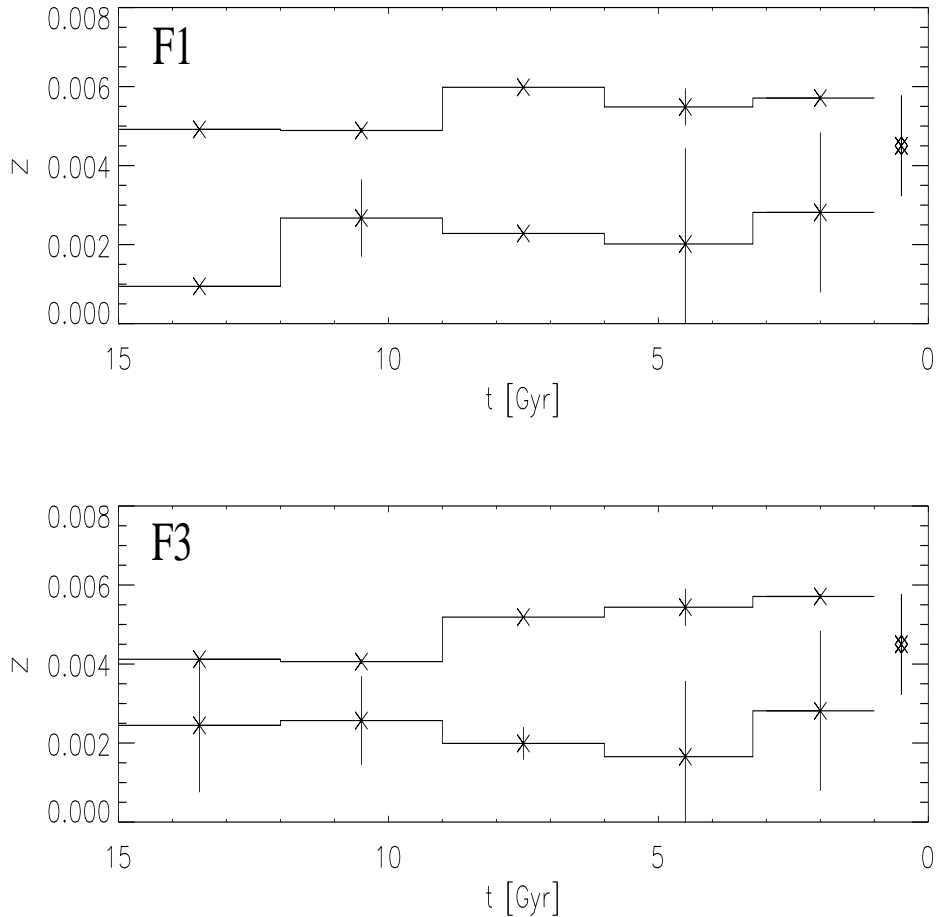


Fig. 9.— The derived variation in heavy element content during the lifetime of NGC 300 for two fields at different radial distances from the galaxy centre. See text in Sec. 7 for further details.

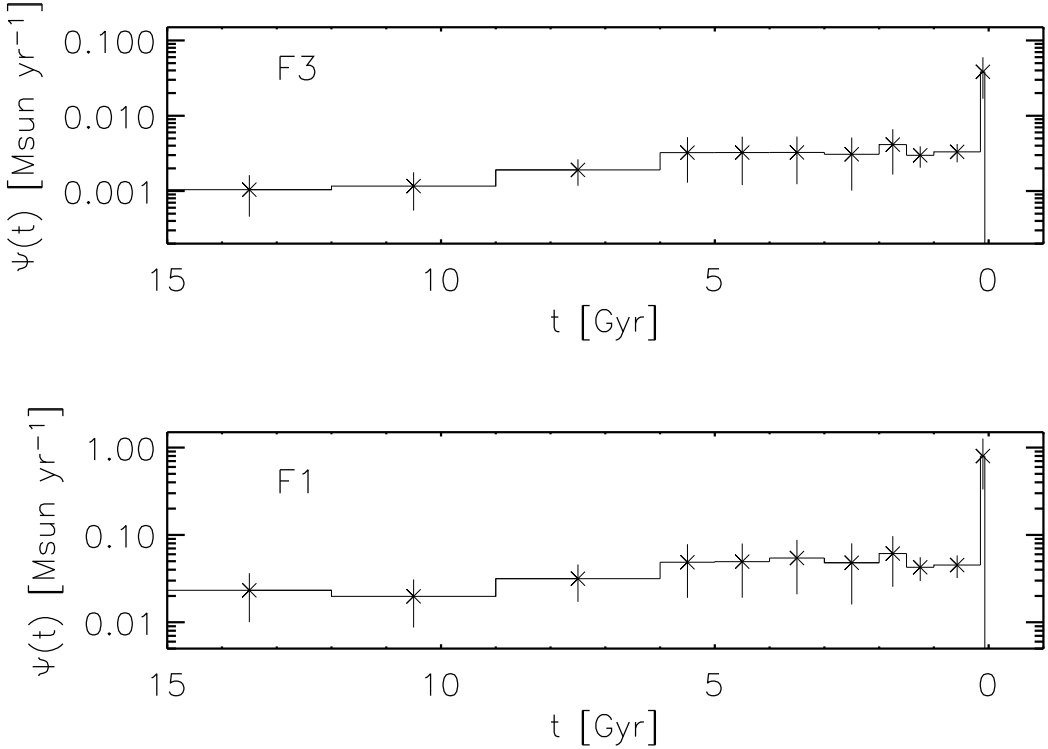


Fig. 10.— SFR solution for two NGC 300 fields using the partial model method, N6E1 (bottom) and centre-off (top). There is a significant star formation rate difference between the two fields. See text in Sec. 7 for further details.

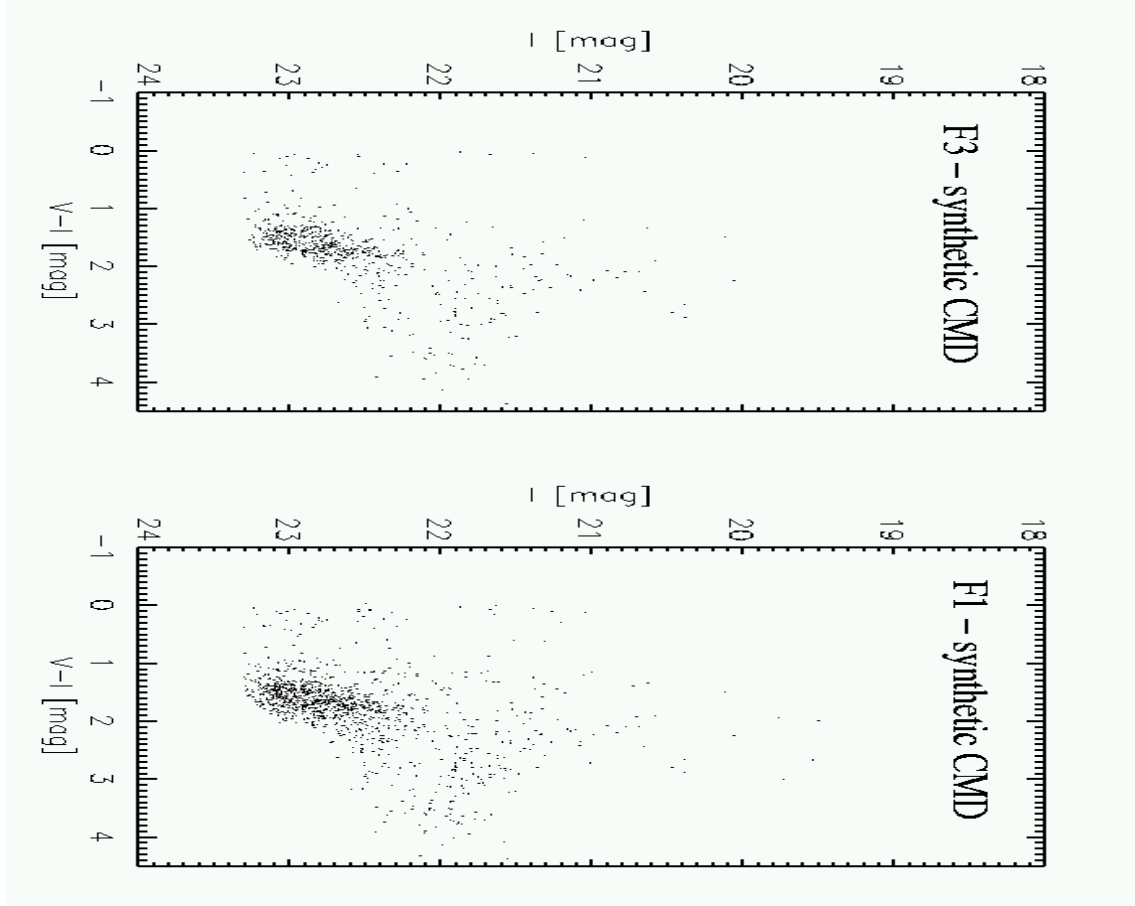


Fig. 11.— Synthetic CMDs for two NGC 300 fields based on the SFH solution in Fig. 10. The CMD has been extended to  $I > 23$  mag, for the sake of presentation, even though the SFR has been determined using stars brighter than this. See text in Sec. 7 for further details.

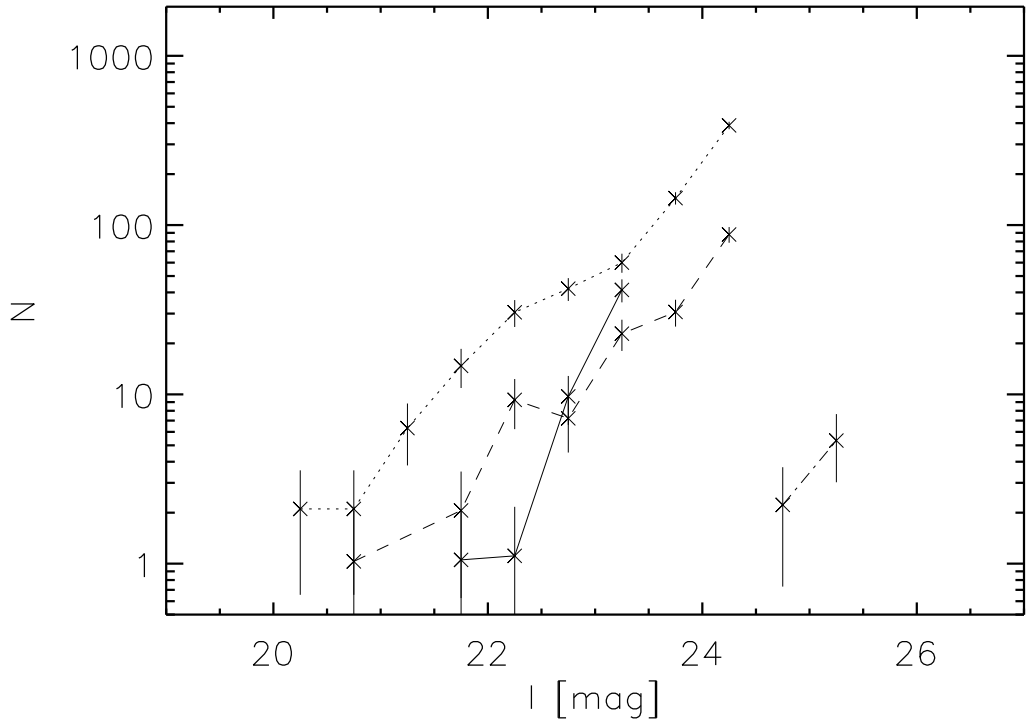


Fig. 12.— I-band luminosity functions for four WFPC2 fields, corrected for incompleteness, for stars above the 50% completeness threshold with  $V-I < 0.6$  (mag). These fields are F1 (*dotted*), F2 (*solid*), F3 (*dashed*), and F4 (*dot-dashed*). Error bars are  $\pm\sqrt{N}$ . See text in sub-Sec. 8 for further details.